Creating Multiple Parallel Internal Phase-junctions on ZnS Nanoparticles as Highly Active Catalytic Sites

Wei Liu, Enna Ha, Luyang Wang, Liangsheng Hu, Lawrence Yoon Suk Lee,* and Kwok-Yin Wong*

Abstract: Semiconductors based on earth-abundant elements such as ZnS are economic materials for energy conversion but are often limited by their light absorption property and fast charge recombination. Herein, we report a solvothermal preparation of ZnS nanocrystals with multiple internal phase-junctions (MIPs) of alternating wurtzite and sphalerite phases, which exhibit dramatically enhanced photocatalytic hydrogen evolution reaction (HER) rate (6.9 mmol g^{-1} h^{-1}) under simulated sunlight. X-ray photoelectron spectroscopy indicated zinc atoms of different electronic environment on the surface of ZnS. The MIP-rich ZnS has substantially lower overpotential for electrocatalytic HER, probably due to the synergistic effect of easier H^+ adsorption and enhanced H_2 desorption on the active sites. This work paves a new route of reforming nanomaterials to acquire intrinsically enhanced catalytic properties for energy conversion applications.

ZnS which consists of only earth-abundant elements of low toxicity is one of the most studied semiconductors for photocatalytic reactions, such as hydrogen generation from water[1] and photoreduction of CO_2,[2] and gaseous pollutants.[3] Despite fairly high theoretical efficiency of photoexciton generation, its large bandgap (~3.7 eV) and fast recombination of charge carriers limit the photocatalytic performance of ZnS, in particular solar-to-hydrogen conversion efficiency. Several strategies, including metal ion doping[1b, 1c, 4] and sulfur vacancy creation,[5] have been developed to suppress the charge recombination and narrow down the bandgap of ZnS. Heterojunctions formed by coupling with narrower band gap semiconductors[6] or plasmonic metal nanoparticles[1a, 7] broaden its photoresponse to the visible-light region. Moreover, the extended heterojunctions in hybrid nanostructures, such as Janus and core-shell structures,[8] can effectively separate the charge carriers.

Recently, the 'homojunction', an internal interface between two different crystal phases, has been reported to boost the photocatalytic activities of Ga_2O_3,[9] ZnS,[10] and $Cd_{1-x}Zn_xS$.[11] The internal electrostatic field formed at these phase-junctions was associated with type-II staggered bandgap alignment that facilitates the spatial separation and transfer of photogenerated charges.[8d, 12] With various polymorphs available, the construction of such internal phase-junctions in metal sulfides can be an effective approach for tuning their band structure to better separate the charge carriers. Nevertheless, how to introduce these phase junctions into the semiconducting materials in a systematic and rational manner is still a big challenge. Herein, we demonstrate a simple two-step method of constructing multiple internal phase junctions (MIPs) in ZnS nanoparticles, where sphalerite (Sp) and wurtzite (Wz) phases coexist as alternating parallel layers. Regularly alternating MIPs have been reported to be highly desirable for the effective transfer and separation of charge due to new electronic states leading to the pinned Fermi level in the energy gap.[13] The Fermi level difference at the parallel phase-junctions can act as a localized electric field that drives directional migration and separation of electron-hole pairs.[11, 14] The density of MIP prepared by this two-step method is readily tunable and correlated to effective promotion of charge separation and transfer, thus contributed to a significant improvement of photocatalytic hydrogen evolution reaction (HER) rate. The rational design of such parallel MIPs in photocatalysts presents a promising strategy for enhancing the photocatalytic activity without introducing any foreign, usually either toxic or rare, components as required by conventional heterojunctions.

ZnS-ethylenediamine ($ZnS(en)_{0.5}$) was first prepared by solvothermal method as a precursor for ZnS nanocrystal. The X-ray diffraction (XRD) pattern of as-obtained $ZnS(en)_{0.5}$ (**Figure S1a** in the supporting information) was indexed to orthorhombic structure, which agrees well with literature.[15] Scanning electron microscope (SEM) and transmission electron microscope (TEM) analyses (**Figure S1b** and **c**) show its plate-like morphology, which was further revealed to comprise numerous nanocrystals (d = 5.3 ± 1.2 nm) by high-resolution TEM (HR-TEM, **Figure S1d**). As both sulfur source and protecting ligand, *L*-cysteine was used which coordinates with metal ions and forms stable complexes. Under the solvothermal conditions used, initially formed Zn^{2+}-cysteine complex gradually dissociates to Zn^{2+} and S^{2-} ions, stabilizing the nucleation and growth of $ZnS(en)_{0.5}$.[16] The ethylenediamine intercalates between two ZnS layers, constructing a plate-like morphology by multiple stacking, as indicated by the sharp XRD peak at 10.2°.[15b, 17]

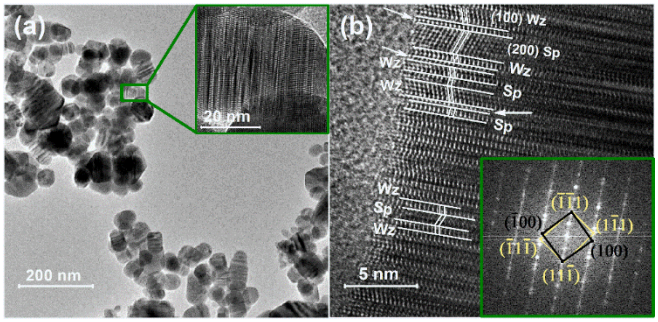

Figure 1. (a) TEM image of ZS-3 ZnS nanocrystals. Inset is a close-up image of the region with MIPs. (b) HR-TEM image of ZS-3. The lines are the interfaces between Wz and Sp phases, and the arrows indicate sandwiched interfaces. Inset shows the fast Fourier transform (FFT) pattern.

$ZnS(en)_{0.5}$ was further treated at various temperatures (from 140 to 260 °C) under hydrothermal conditions, which induced the decomposition of $ZnS(en)_{0.5}$ into smaller and round-shaped ZnS nanocrystals. Depending on the hydrothermal temperature, *in situ* nucleation and atomic rearrangement lead to not only different shapes but also different crystal phases of ZnS.[6b, 18] **Figure S2** compares the TEM images of four ZnS nanocrystals obtained at 140, 180, 220, and 260 °C, labeled as ZS-1, ZS-2, ZS-3, and ZS-4, respectively. The size of ZnS nanocrystals show an increasing

* W.L.; E.H.; L.W.; L.H; L.Y.S.L.; K.-Y.W;
Department of Applied Biology and Chemical Technology and the State Key Laboratory of Chirosciences
The Hong Kong Polytechnic University
Hung Hom, Kowloon, Hong Kong SAR, China
E-mails: lawrence.ys.lee@polyu.edu.hk (L.Y.S. Lee);
kwok-yin.wong@polyu.edu.hk (K.-Y. Wong)

Supporting information for this article is given via a link at the end of the document.

trend with hydrothermal temperature, ranging from 36.5 to 133.1 nm. The particle growth could be caused by the crystal ripening or aggregation process when the temperature increased.[18b] More interestingly, we observed stripe-like interfaces, the density of which generally increases with reaction temperature (**Figure S3**); the average interface length per particle increases from 1.5 nm for ZS-1 to a maximum of 7.4 nm for ZS-3, but decreases slightly to 5.2 nm for ZS-4. **Figure 1** shows the TEM and HR-TEM images of ZS-3 where dual crystal phases are clearly revealed by distinctive lattice fringes; the lattice spacings of 0.33 and 0.27 nm are ascribed to the (100) plane of wurtzite (Wz) phase and the (200) plane of sphalerite (Sp) phase, respectively. These Wz and Sp phases are periodically alternating, thus forming multiple parallel interfaces over most of nanocrystal surface. The associated fast Fourier transform (FFT) pattern also supports this polytype nature with organized Sp and Wz phases (inset in **Figure 1(b)**).[19a,19b] We also observed a few twisted lattice fringes (indicated with arrow in **Figure 1(b)**) that constitute a sandwiched interface and may serve as a transitional state between the Sp-Wz heterophase. Such stripe-like MIPs may result from the atomic rearrangement as a transitional state between two crystalline phases, which have a mean surface energy difference of 0.22 J m^{-2}.[10, 19c]

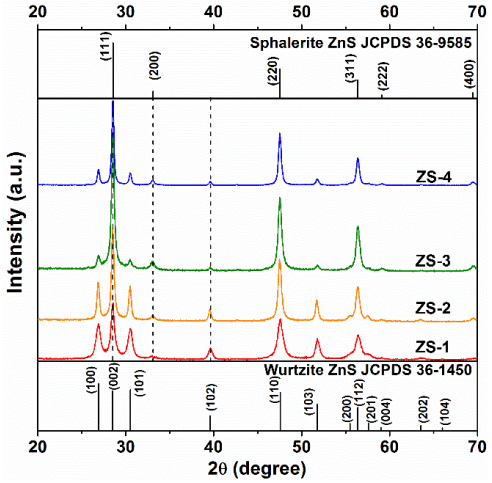

Figure 2. XRD patterns of ZnS nanocrystals synthesized at various hydrothermal temperatures (ZS-1: 140 °C; ZS-2: 180 °C; ZS-3: 220 °C; ZS-4: 260 °C).

To investigate the crystalline structure and phase composition, powder XRD was employed and the patterns are shown in **Figure 2**. ZS-1 shows a characteristic diffraction pattern indexed to hexagonal Wz phase ZnS (JCPDS No.36-1450) with a small peak at 33.1° suggesting the existence of Sp phase. It is noteworthy that thermodynamically metastable Wz phase was obtained in ZS-1 at 140 °C, which is usually formed only at > 400 °C.[20] This could be related to the Zn^{2+}-cysteine complex that has been shown to have the favorable surface energy, thus stabilizes the formation of metastable Wz phase ZnS at low temperature.[21] The ZnS nanocrystals prepared at higher temperatures, ZS-2 and ZS-3, show similar XRD patterns as ZS-1. The relative intensity of peak at 28.6°, however, increased sharply, which can be ascribed to both (111) plane of Sp phase and (002) plane of Wz phase. Such acute increase in peak intensity, in contrast to its two neighbor peaks (26.9 and 30.5°), suggests the substantial contribution from Sp phase. The formation of MIP can create plenty of dangling bonds along the direction of (111) plane of Sp phase and (002) plane of Wz phase, which lead to new electronic states on the surface of ZnS nanocrystal.[22] In addition, the peaks at 33.1 and 39.6° also indicates the co-existence of Wz and Sp phases. The hydrothermal extraction of ethylenediamine from the $ZnS(en)_{0.5}$ by the strong solvation of water is believed to lead to the surface atomic rearrangement and the formation of dual phase.[10, 23] Meanwhile, ZS-4 exhibits decreased intensities from (111) and (200) planes of Sp-phase, which could result from the transformation of interface states at a high temperature.[24] It is evident that the reaction temperature modulates the phase evolutions in ZnS and the growth of thermodynamically stable phase-junctions.

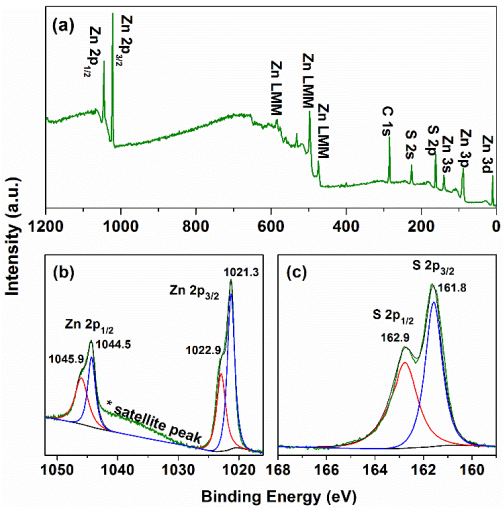

Figure 3. (a) XPS survey spectra of ZS-3 and high-resolution XPS spectra of (b) Zn 2p and (c) S 2p.

The coexistence of Wz and Sp phases is also supported by the characteristic phonon modes in Raman spectroscopy (**Figure S4**). The broad band at 218 cm^{-1} and bands at 253 cm^{-1} (A_1, E_1) and 304 cm^{-1} (E_L^2) can be assigned to the longitudinal acoustic overtone and polar modes observed in Wz phase of ZnS, respectively.[25] The longitudinal optical mode located at 351 cm^{-1} (T_2) is consistent with previous reports of the characteristic Sp phase in ZnS.[26] Notably, the band at 267 cm^{-1} becomes prominent in ZS-3 and it merges with the band at 253 cm^{-1} in ZS-4, which is a clear indication of the transverse optical mode of Sp phase ZnS.[25] In the high-frequency region (550 - 800 cm^{-1}), the optical overtone and combinational bands at 617, 642, and 671 cm^{-1} are typical for Sp phase of ZnS (inset in **Figure S4**).[27]

In order to have further insights on the MIP, the surface composition and chemical states of ZS-3 were examined by X-ray photoelectron spectroscopy (XPS) analysis. The XPS survey spectrum shown in **Figure 3(a)** identifies the presence of Zn and S on the surface with no other impurities. Contrary to the common ZnS 2p XPS spectrum where two single peaks corresponding to Zn $2p_{1/2}$ and $2p_{3/2}$ are observed, the Zn 2p HR-XPS spectrum of ZS-3 exhibits two split peaks corresponding to Zn $2p_{1/2}$ and $2p_{3/2}$, suggesting different electronic environments for Zn atoms (**Figure 3(b)**). The major Zn $2p_{1/2}$ and $2p_{3/2}$ peaks with lower binding energies of 1044.5 and 1021.3 eV, respectively, can be related to the electron-rich Zn^{2+} due to the Zn-Zn misalignment near MIPs, whereas the minor peaks with higher binding energies of 1045.9 and 1022.9 eV are due to surface Zn^{2+} species with low-coordination number and stronger metallic character.[17] The different electronic environments of Zn species, which usually

arise from the surface bonding faults or local surface disorder on surface, lead to splitting peaks.[5] At the engaged hydrothermal temperatures, the ethylenediamine molecules are released from the layer-structured precursor under kinetic control, which is believed to leave non-uniform surfaces that form the parallel interfaces between phases,[28] and thus cause the surface Zn-S bonding faults, leading to different chemical states of Zn and S.[29] Meanwhile, two split peaks for S located at 161.8 and 160.4 eV are assigned to S $2p_{1/2}$ and S $2p_{3/2}$ (**Figure 3(c)**), which is consistent with the reported values.[30]

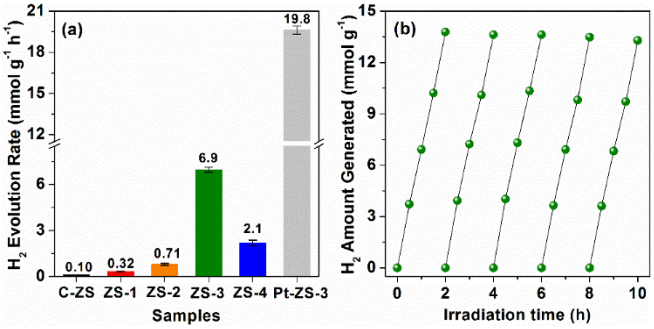

Figure 4. (a) Photocatalytic hydrogen generation rates of ZnS nanocrystals prepared at various hydrothermal temperatures (ZS-1 to ZS-4). Commercial ZnS nanocrystal (C-ZS) and Pt nanoparticle decorated ZS-3 (Pt/ZS-3) are shown for comparison. (b) Stability test for photocatalytic cycles of ZS-3. All measurements were carried out with a 100 mW cm^{-2} solar simulator.

The MIP, as a line of defects, can alter the physicochemical properties of nanocrystals by lowering the energy barriers. We first investigated the effects of MIPs on the optical properties of ZnS nanocrystals by UV-Vis diffuse reflectance spectroscopy. All four samples exhibit the absorption cut-offs at ~375 nm (**Figure S5**), which are red-shifted from that of the commercial ZnS (C-ZS, 343 nm). The corresponding bandgap energy (E_g) calculated by the transformed Kubelka−Munk function and the Tauc plot (inset in **Figure S5**) yields the E_g of *ca*. 3.4 eV, slightly lower than that of C-ZS (3.6 eV). The narrower bandgap is apparent in the spectra of ZS-1 and ZS-2 with broad absorption bands tailing off to 800 nm. Therefore, the formation of MIPs induces bond distortions that lead to localized electronic levels in the forbidden band gap.[31] ZS-3 and ZS-4, however, show only subtle changes in the visible range absorption, probably due to the increased local surface disorder.[32]

With modified atomic arrangements and optical properties, it is of great interest to find out how these aligned MIPs affect the photocatalytic activity of ZnS. The photocatalytic HER was carried out under simulated solar illumination using 0.35 M Na_2S + 0.25 M Na_2SO_3 solution as sacrificial agent and the results are summarized in **Figure 4(a)**. The C-ZS showed poor photocatalytic HER rate of merely 0.10 mmol g^{-1} h^{-1}, which is expected for its limited light absorption and fast recombination of charge carriers.[33] On the contrary, all ZnS nanocrystals with MIPs show significantly enhanced HER rates. ZS-1 and ZS-2 generate H_2 at the rates of 0.32 and 0.71 mmol g^{-1} h^{-1}, which account for 320 and 710 % enhancement from C-ZS, respectively. The most MIP-rich ZS-3 shows an exceptionally high HER rate of 6.9 mmol g^{-1} h^{-1} with an apparent quantum efficiency (AQE) of 36.8 %. This outperforms most, if not all, of the literature reported ZnS-based photocatalytic systems for HER under simulated sunlight (**Table S1**). More importantly, such high HER rate was achieved without the assistance of any co-catalyst or support. As suggested by TEM images, the enhanced photocatalytic activity of ZS-3 is associated with the highest density of alternating Sp-Wz interfaces, which may form ordered type-II energy band alignments to effectively drive the spatial separation of photogenerated charge carriers. Such parallel interfaces are known to eliminate the charge recombination centers and facilitate the transport of charge carriers.[34] Moreover, the MIPs along (111) plane of Sp phase and (002) plane of Wz phase possess a lower potential barrier, which would help charge localization and migration out by a tunneling process to the surface for H_2 generation.[35]

To shed light on the active sites, we carried out the photo-reduction of metal ions on ZS-3. H_2PtCl_6 was selected as a metal salt based on the lower Fermi level of Pt, compared with other noble metals, to trap electrons from the surface of ZS-3. The electrons were released for H_2 evolution due to the lowest activation energy of Pt.[36] After 30 min of irradiation, Pt nanoparticles (average d = 4.2 nm) were formed mostly on the edges and MIPs, indicating electron-rich nature of those sites for reduction reaction (**Figure S7**). With 0.3 wt% Pt nanoparticles loaded, the photocatalytic HER rate of ZS-3 was further boosted to 19.8 mmol g^{-1} h^{-1}, a 2.8-fold enhancement from the bare ZS-3 and nearly 200 times higher than C-ZS. To the best of our knowledge, this is among the highest HER rates of metal sulfide-based photocatalysts reported up to date. The photocatalytic performance of ZS-4 is, however, substantially lower (2.1 mmol g^{-1} h^{-1}) than that of ZS-3, presumably due to the collective effects of increased particle size and decreased MIP density. The HER activity of studied samples correlates well with the average interface length (**Figure S4**). In a continuous 10 h reaction to test long term photo-stability, no significant loss of activity was observed (**Figure 4(b)**), and the subsequent TEM analysis confirmed no structural changes nor aggregation occurred during HER, both of which demonstrate good stability of ZS-3 (**Figure S8**). Meanwhile, under visible light illumination (λ ≥ 420 nm), the HER rate of ZS-3 drops to 21.7 μmol g^{-1} h^{-1}, suggesting that the enhancement is not due to the improved light absorption, but better utilization of excited charges.

In addition to photocatalysis, a parallel investigation of electrocatalytic properties can provide more information on the proton adsorption for H_2 formation at ZnS nanocrystal surface. The ZnS nanocrystals were drop-cast onto the glassy carbon electrode (GCE) with 5 wt% Nafion and used as the working electrode in a typical three-electrode setup (**Figure S9**). **Figure 5** compares the HER polarization curves of ZnS samples, C-ZS, and Pt on graphitized carbon (20 wt% Pt/C) measured in 0.5 M H_2SO_4 at a scan rate of 1 mV s^{-1}. In the studied potential range (50 to -550 mV), C-ZS shows the lowest electrocatalytic activity with an onset potential of -370 mV (*vs*. RHE). By contrast, all ZnS samples with MIPs show considerable improvements in electrocatalytic performances, as summarized in **Table S2**. In particular, ZS-3 exhibits the best electrocatalytic properties with a current density of -9.3 mA cm^{-2} at -0.3 V and an onset potential of -100 mV, which accounts ~270 mV improvement in overpotential and *ca*. 70-fold increase in current density from C-ZS. It is noteworthy that the electrocatalytic performance of ZnS nanocrystals is consistent with their photocatalytic activities and can be further correlated to the phase-junctions on the surface.[37b] In general, the current density increases and the corresponding onset potential decreases with the MIP density. This trend is also noted from the Tafel plot (**Figure S10**) where the slope of the curve reflects the activity of catalytic reaction. It clearly suggests

that the MIP formation on ZnS significantly benefits the catalytic performance for HER by promoting surface charge transport and enriching the localized electron density.[36-37] In electrocatalytic HER, protons from the medium are first adsorbed onto the ZnS surface and form adsorbed species (H_{ads}), which is known as Volmer reaction: $H_3O^+ + e^- \rightarrow H_{ads} + H_2O$.[38] The electrons driven by applied potential reduce the H_{ads} into H_2 through an electrochemical desorption step (Heyrovsky reaction): $H_{ads} + H_3O^+ + e^- \rightarrow H_2 + H_2O$. As the MIPs are suggested to facilitate the charge transport, the desorption step occurs at lower overpotentials. Moreover, the increased current density of MIP-rich ZnS indicates lower resistivity to conduction electrons and expanded capacity for H^+ adsorption on the surface.[39]

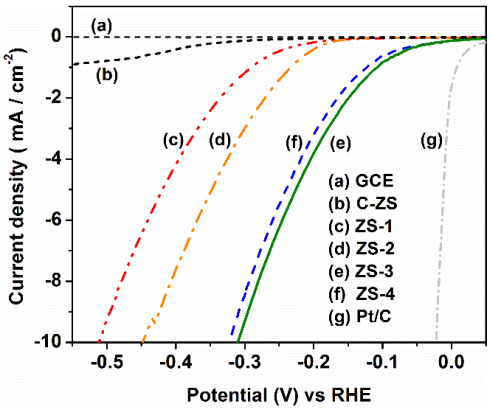

Figure 5. Polarization curves of ZnS samples for HER. ZnS samples are compared with bare GCE, commercial ZnS (C-ZS), and 20 wt% Pt on graphitized carbon (Pt/C).

In conclusion, multiple internal interfaces of alternating Wz and Sp phases are constructed on ZnS nanocrystals by a simple two-step method. The size and dominating phase of ZnS nanocrystals as well as the density of phase-junction are readily tunable. The existence of aligned Wz/Sp interfaces effectively facilitates the charge carrier separation and photoelectron localization for surface reaction, hence remarkably promotes photocatalytic HER performance of ZnS to 6.9 mmol g^{-1} h^{-1}. The electrocatalytic HER results also indicate the facilitated charge transport and easier proton adsorption in the MIP-rich ZnS nanocrystals. This work demonstrates that internal interface engineering can be an effective strategy to realize highly-efficient co-catalyst-free photocatalytic H_2 generation.

Experimental Section

Sample preparation: $ZnS(en)_{0.5}$ (en = ethylenediamine) was first prepared as a precursor for ZnS nanocrystals using an ethylenediamine-mediated solvothermal method, according to the literature with slight modifications.[10, 30b, 40] Subsequent hydrothermal treatment of the $ZnS(en)_{0.5}$ yielded the ZnS nanocrystals with phase-junctions. In a typical synthesis, 2 mmol $Zn(OAc)_2$ and 4 mmol *L*-cysteine were dispersed in 30 mL ethylenediamine. The mixture was transferred to a 50-mL Teflon-lined stainless-steel autoclave and heated at 180 °C for 24 h. The precursor obtained as precipitate was collected by centrifuge, washed with deionized water and ethanol for three times, and dried in a vacuum oven at 50 °C. 50 mg of dried precursor was dispersed in 30 mL water and hydrothermally treated at various temperatures for 12 h.

Sample characterization: Crystal structure of samples was identified by X-ray diffraction (XRD, Rigaku SmartLab) with a diffraction angle (2θ) ranging from 10 to 70°. Transmission electron microscope (TEM) images were obtained using a STEM (JEOL JEM-2100F) operated with a field emission gun at 200 kV. The samples were first dispersed in ethanol and drop-cast onto holey carbon-coated 400 mesh copper grids. The UV–vis diffuse reflectance spectroscopy was recorded using a UV–Vis spectrophotometer (Cary 4000) with ultrapure $BaSO_4$ as the background. Raman spectra were obtained by a Raman spectrometer (Renishaw inVia) with the excitation wavelength of 785 nm at room temperature. X-ray photoelectron spectroscopy (XPS) measurements were performed using a K-Alpha X-ray photoelectron spectrometer (Thermo Fisher Scientific, UK) with a monochromatic Al Kα X-ray source (excitation energy = 1,468.6 eV) and a base pressure of 3×10^{-9} Torr in the analytical chamber. Electrochemical measurements were performed using a 1030A CHI electrochemical workstation. 3 mg catalyst and 20 μL 5 wt% Nafion solution were dispersed in 2 mL water/ethanol (3:1 v/v) by 10 min sonication to form homogeneous suspension. Then, 10 μL catalyst ink was drop-cast onto a glassy carbon electrode of 3 mm diameter (surface area = 0.07 cm^2) as the working electrode with a constant mass loading of 0.21 mg cm^{-2}. A linear sweep voltammogram from 0 to -0.6 V was measured at a scan rate of 1 mV s^{-1} in 0.5 M H_2SO_4 using a saturated calomel electrode and a Pt wire as the reference electrode and counter electrode, respectively.

Photocatalytic Activity Test: In a typical run, 5 mg sample was suspended in 25 mL of 0.35M Na_2S + 0.25M Na_2SO_3 aqueous solution under stirring, and irradiated with a Newport solar simulator (150 W Xe lamp, ozone free, Air Mass Filter, AM 1.5 Global) of 100 mW/cm^2 light intensity for 1 h. The amount of generated H_2 was analyzed by Agilent 7890B gas chromatograph system equipped with a TCD detector using N_2 as carrier gas.

Acknowledgements

We acknowledge support from the Innovation and Technology Commission of Hong Kong and the Hong Kong Polytechnic University. K.-Y.W. acknowledges the support from the Patrick S.C. Poon Endowed Professorship.

Keywords: photocatalysis • hydrogen evolution reaction • internal phase-junction • ZnS nanocrystal • charge carrier

[1] (a) J. Zhang, Y. Wang, J. Zhang, Z. Lin, F. Huang, J. Yu, *ACS Appl. Mater. Interfaces* **2013**, *5*, 1031-7; (b) T. Arai, S.-i. Senda, Y. Sato, H. Takahashi, K. Shinoda, B. Jeyadevan, K. Tohji, *Chem. Mater.* **2008**, *20*, 1997-2000; (c) J. Zhang, S. Liu, J. Yu, M. Jaroniec, *J. Mater. Chem.* **2011**, *21*, 14655-62; (d) J. Yu, J. Zhang, S. Liu, *J. Phys. Chem. C* **2010**, *114*, 13642-9; (e) I. Tsuji, H. Kato, A. Kudo, *Angew. Chem. Int. Ed.* **2005**, *44*, 3565-8; (f) Y. Li, G. Chen, Q. Wang, X. Wang, A. Zhou, Z. Shen, *Adv. Funct. Mater.* **2010**, *20*, 3390-8.

[2] (a) X. Meng, Q. Yu, G. Liu, L. Shi, G. Zhao, H. Liu, P. Li, K. Chang, T. Kako, J. Ye, *Nano Energy* **2017**, *34*, 524-32; (b) R. Zhou, M. I. Guzman, *J. Phys. Chem. C* **2014**, *118*, 11649-56; (c) T. Baran, S. Wojtyła, A. Dibenedetto, M. Aresta, W. Macyk, *Appl. Catal., B Environ.* **2015**, *178*, 170-6.

[3] B. Liu, X. Hu, X. Li, Y. Li, C. Chen, K.-h. Lam, *Sci. Rep.* **2017**, *7*, 16396.

[4] (a) A. Kudo, M. Sekizawa, *Catalysis Letters* **1999**, *58*, 241-3; (b) A. Kudo, M. Sekizawa, *Chem. Commun.* **2000**, 1371-2.

[5] G. Wang, B. Huang, Z. Li, Z. Lou, Z. Wang, Y. Dai, M.-H. Whangbo, *Sci. Rep.* **2015**, *5*, 8544.

[6] (a) I. Tsuji, H. Kato, H. Kobayashi, A. Kudo, *J. Am. Chem. Soc.* **2004**, *126*, 13406-13; (b) J. Zhang, J. Yu, Y. Zhang, Q. Li, J. R. Gong, *Nano Lett.* **2011**, *11*, 4774-9; (c) B. Zhu, B. Lin, Y. Zhou, P. Sun, Q. Yao, Y. Chen, B. Gao, *J. Mater. Chem. A* **2014**, *2*, 3819-27; (d) Y. Hong, J. Zhang, F. Huang, J. Zhang, X. Wang, Z. Wu, Z. Lin, J. Yu, *J. Mater. Chem. A* **2015**, *3*, 13913-9.

[7] S. R. Chalana, V. Ganesan, V. P. M. Pillai, *AIP Adv.* **2015**, *5*, 107207.

[8] (a) Z. W. Seh, S. Liu, M. Low, S.-Y. Zhang, Z. Liu, A. Mlayah, M.-Y. Han, *Adv. Mater.* **2012**, *24*, 2310-4; (b) E. Ha, L. Y. S. Lee, J. Wang, F. Li, K.-Y. Wong, S. C. E. Tsang, *Adv. Mater.* **2014**, *26*, 3496-500; (c) Y.-P. Yuan, L.-W. Ruan, J. Barber, S. C. Joachim Loo, C. Xue, *Energy Environ. Sci.* **2014**, *7*, 3934-51; (d) T.-T. Zhuang, Y. Liu, Y. Li, Y. Zhao, L. Wu, J. Jiang, S.-H. Yu, *Angew. Chem.* **2016**, *128*, 6506-10.

[9] X. Wang, Q. Xu, M. Li, S. Shen, X. Wang, Y. Wang, Z. Feng, J. Shi, H. Han, C. Li, *Angew. Chem. Int. Ed.* **2012**, *51*, 13089-92.

[10] Z. Fang, S. Weng, X. Ye, W. Feng, Z. Zheng, M. Lu, S. Lin, X. Fu, P. Liu, *ACS Appl. Mater. Interfaces* **2015**, *7*, 13915-24.

[11] M. Liu, D. Jing, Z. Zhou, L. Guo, *Nat. Commun.* **2013**, *4*, 2278.

[12] R. E. Algra, M. A. Verheijen, M. T. Borgstrom, L.-F. Feiner, G. Immink, W. J. P. van Enckevort, E. Vlieg, E. P. A. M. Bakkers, *Nature* **2008**, *456*, 369-72.

[13] (a) K. Pemasiri, M. Montazeri, R. Gass, L. M. Smith, H. E. Jackson, J. Yarrison-Rice, S. Paiman, Q. Gao, H. H. Tan, C. Jagadish, X. Zhang, J. Zou, *Nano Lett.* **2009**, *9*, 648-54; (b) M. Liu, Y. Chen, J. Su, J. Shi, X. Wang, L. Guo, *Nat. Energy* **2016**, *1*, 16151; (c) W. E. Spicer, I. Lindau, P. Skeath, C. Y. Su, P. Chye, *Phys. Rev. Lett.* **1980**, *44*, 420-3.

[14] C. R. M. Grovenor, *J. Phys. C: Solid State Phys.* **1985**, *18*, 4079.

[15] (a) S.-H. Yu, M. Yoshimura, *Adv. Mater.* **2002**, *14*, 296-300; (b) X. Ouyang, T.-Y. Tsai, D.-H. Chen, Q.-J. Huang, W.-H. Cheng, A. Clearfield, *Chem. Commun.* **2003**, 886-7.

[16] H. Du, K. Liang, C.-Z. Yuan, H.-L. Guo, X. Zhou, Y.-F. Jiang, A.-W. Xu, *ACS Appl. Mater. Interfaces* **2016**, *8*, 24550-8.

[17] W. Feng, Z. Fang, B. Wang, L. Zhang, Y. Zhang, Y. Yang, M. Huang, S. Weng, P. Liu, *J. Mater. Chem. A* **2017**, *5*, 1387-93.

[18] (a) Z.-X. Deng, C. Wang, X.-M. Sun, Y.-D. Li, *Inorg. Chem.* **2002**, *41*, 869-73; (b) M. Uehara, Y. Nakamura, S. Sasaki, H. Nakamura, H. Maeda, *CrystEngComm* **2011**, *13*, 5998-6001.

[19] (a) X. Wang, J. Shi, Z. Feng, M. Li, C. Li, *Phys. Chem. Chem. Phys.* **2011**, *13*, 4715-23; (b) Z. Wu, X. Sun, H. Xu, H. Konishi, Y. Wang, Y. Lu, K. Cao, C. Wang, H. Zhou, *Ore Geol. Rev.* **2018**, *92*, 318-47; (c) Z. Wang, L. L. Daemen, Y. Zhao, C. S. Zha, R. T. Downs, X. Wang, Z. L. Wang, R. J. Hemley, *Nat. Mater.* **2005**, *4*, 922.

[20] Y. Cuizhuo, L. Yanguo, S. Hongyu, G. Defeng, L. Xiaohong, L. Wei, L. Baoting, Z. Xiangyi, *Nanotech.* **2008**, *19*, 095704.

[21] X. Wu, K. Li, H. Wang, *J. Alloys Compd.* **2009**, *487*, 537-44.

[22] D. J. Chadi, *Phys. Rev. Lett.* **1979**, *43*, 43-7.

[23] G.-T. Zhou, X. Wang, J. C. Yu, *Cryst. Growth Des.* **2005**, *5*, 1761-5.

[24] F. Huang, J. F. Banfield, *J. Am. Chem. Soc.* **2005**, *127*, 4523-9.

[25] S. A. Acharya, N. Maheshwari, L. Tatikondewar, A. Kshirsagar, S. K. Kulkarni, *Cryst. Growth Des.* **2013**, *13*, 1369-76.

[26] O. Brafman, S. S. Mitra, *Phy. Rev.* **1968**, *171*, 931-4.

[27] Y. C. Cheng, C. Q. Jin, F. Gao, X. L. Wu, W. Zhong, S. H. Li, P. K. Chu, *J. Appl. Phys.* **2009**, *106*, 123505.

[28] H.-B. Kim, D.-J. Jang, *Nanoscale* **2016**, *8*, 403-10.

[29] (a) A. Malakar, B. Das, S. Islam, C. Meneghini, G. De Giudici, M. Merlini, Y. V. Kolen'ko, A. Iadecola, G. Aquilanti, S. Acharya, S. Ray, *Sci. Rep.* **2016**, *6*, 26031; (b) W. Vogel, P. H. Borse, N. Deshmukh, S. K. Kulkarni, *Langmuir* **2000**, *16*, 2032-7.

[30] (a) E. Ha, W. Liu, L. Wang, H.-W. Man, L. Hu, S. C. E. Tsang, C. T.-L. Chan, W.-M. Kwok, L. Y. S. Lee, K.-Y. Wong, *Sci. Rep.* **2017**, *7*, 39411; (b) X. Yang, H. Xue, J. Xu, X. Huang, J. Zhang, Y. B. Tang, T. W. Ng, H. L. Kwong, X. M. Meng, C. S. Lee, *ACS Appl. Mater. Interfaces* **2014**, *6*, 9078-84.

[31] F. A. La Porta, J. Andres, M. S. Li, J. R. Sambrano, J. A. Varela, E. Longo, *Phys. Chem. Chem. Phys.* **2014**, *16*, 20127-37.

[32] H. Yaghoubi, Z. Li, Y. Chen, H. T. Ngo, V. R. Bhethanabotla, B. Joseph, S. Ma, R. Schlaf, A. Takshi, *ACS Catal.* **2015**, *5*, 327-35.

[33] X. Chen, S. Shen, L. Guo, S. S. Mao, *Chem. Rev.* **2010**, *110*, 6503-70.

[34] (a) P. T. Landsberg, M. S. Abrahams, *J. Appl. Phys.* **1984**, *55*, 4284-93; (b) M. Liu, L. Wang, G. Lu, X. Yao, L. Guo, *Energy Environ. Sci.* **2011**, *4*, 1372-8.

[35] Y. Hou, A. B. Laursen, J. Zhang, G. Zhang, Y. Zhu, X. Wang, S. Dahl, I. Chorkendorff, *Angew. Chem. Int. Ed.* **2013**, *52*, 3621-5.

[36] J. Yang, D. Wang, H. Han, C. Li, *Acc. Chem. Res.* **2013**, *46*, 1900-9.

[37] (a) D. R. Cummins, U. Martinez, A. Sherehiy, R. Kappera, A. Martinez-Garcia, R. K. Schulze, J. Jasinski, J. Zhang, R. K. Gupta, J. Lou, M. Chhowalla, G. Sumanasekera, A. D. Mohite, M. K. Sunkara, G. Gupta, *Nat. Commun.* **2016**, *7*, 11857; (b) S. Liu, Z. Zhang, J. Bao, Y. Lan, W. Tu, M. Han, Z. Dai, *J. Phys. Chem. C* **2013**, *117*, 15164-73

[38] (a) E. Skulason, G. S. Karlberg, J. Rossmeisl, T. Bligaard, J. Greeley, H. Jonsson, J. K. Norskov, *Phys. Chem. Chem. Phys.* **2007**, *9*, 3241-50; (b) K. J. Vetter, *Electrochemical Kinetics: Theoretical and Experimental Aspects*, Academic Press, New York, **1967**.

[39] (a) L. Lu, Y. Shen, X. Chen, L. Qian, K. Lu, *Science* **2004**, *304*, 422-6; (b) B. E. Conway, B. V. Tilak, *Electrochim. Acta* **2002**, *47*, 3571-94.

[40] Y. Kim, J.-Y. Kim, D.-J. Jang, *J. Phys. Chem. C* **2012**, *116*, 10296-302.

Text for Table of Contents

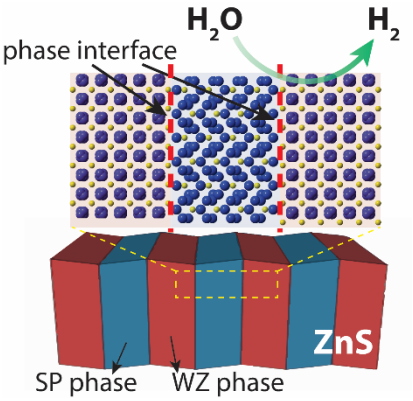

Wei Liu, Enna Ha, Luyang Wang, Liangsheng Hu, Lawrence Yoon Suk Lee and Kwok-Yin Wong**

Page No. – Page No.

Creating Multiple Parallel Internal Phase-junctions on ZnS Nanoparticles as Highly Active Catalytic Sites